Sedimenting elastic filaments in turbulent flows

Rahul K. Singh [1,2,*] Jason R. Picardo [3,†] and Samriddhi Sankar Ray [2,‡]

[1] *Complex Fluids and Flows Unit, Okinawa Institute of Science and Technology Graduate University, Okinawa 904-0495, Japan*

[2] *International Centre for Theoretical Sciences, Tata Institute of Fundamental Research, Bangalore 560089, India*

[3] *Department of Chemical Engineering, Indian Institute of Technology Bombay, Mumbai 400076, India*

(Received 3 January 2021; accepted 8 August 2022; published 23 August 2022)

We investigate the gravitational settling of a long, model elastic filament in homogeneous isotropic turbulence. We show that the flow produces a strongly fluctuating settling velocity whose mean is moderately enhanced over the still-fluid terminal velocity and whose variance has a power-law dependence on the filament's weight but is surprisingly unaffected by its elasticity. In contrast, the tumbling of the filament is shown to be closely coupled to its stretching and manifests as a Poisson process with a tumbling time that increases as a power law with the elastic relaxation time of the filament. Apart from elasticity, inertia, and gravitational acceleration, we have also considered the effect of bending stiffness and found that stiff filaments settle slower but tumble faster than fully flexible filaments.

DOI: 10.1103/PhysRevFluids.7.084502

I. INTRODUCTION

Sediments in turbulent flows, commonplace in nature and industry, raise the question of how objects settle under gravity while being buffeted by a turbulent carrier flow. Even for the simplest case of tiny rigid spherical particles, the interaction of these forces is intricate and leads to an enhancement of the settling velocity over its value in a still fluid [1–7]. Recent work has extended our understanding to spheroidal particles, with additional rotational degrees of freedom, and addressed the issue of how they orient themselves while settling [8,9]. A common feature of these prior studies is that they are limited to rigid particles whose sizes, regardless of their anisotropy, are much smaller than the dissipative Kolmogorov scale η of the flow. These constraints are certainly meaningful for a wide variety of applications, such as understanding the initiation of rain in warm clouds [10–14] and the radiative properties of cold clouds [15–18], which involve, respectively, turbulent suspensions of spherical water droplets and nonspherical ice crystals.

However, sediments that are both deformable and larger than the Kolmogorov scale are just as ubiquitous. One important example is the sedimentation of long deformable filaments, wherein flow-induced deformation modifies the net drag force experienced by the filament [19], thus coupling the dynamics of conformation to settling. This problem has been recently addressed for low Reynolds number, nonturbulent flows [20,21]. However, understanding the gravitational settling of filaments when the carrier flow is turbulent remains an important open problem, encountered in diverse settings such as fiber suspensions in industry [22], sedimentation of passive marine pollutants such

*rksphys@gmail.com

†Associate at the International Centre for Theoretical Sciences, TIFR, India; jrpicardo@che.iitb.ac.in

‡samriddhisankarray@gmail.com

as plastic debris from fishing gear [23–25], as well as the dynamics of filamentary microorganisms in the field of marine ecology [26–28].

In this paper, we address this issue through a combination of scaling analysis and detailed numerical simulations on a model elastic filament in a homogeneous and isotropic turbulent flow. In particular, we show that the turbulent flow produces strong fluctuations in the settling velocity, while moderately enhancing its mean value over the terminal velocity in a still-fluid. We theoretically derive how the normalized variance of the settling velocity scales with the elasticity and inertia (mass) of the filament, as well as with the relative strengths of the accelerations due to gravity and turbulence. Our estimates are then verified through detailed numerical simulations. Furthermore, applying ideas from the persistence problem of nonequilibrium statistical physics, we uncover a close connection between the two internal motions of tumbling and stretching, which accompany the unsteady yet inevitable descent of the filament.

A simple model of a long filament, which retains enough internal structure to exhibit both elasticity and inertia, is a chain of heavy inertial particles connected through elastic springs. Such chains are a macroscopic adaptation of the bead-spring model commonly used to study polymers [29]—a connection suggested by experiments on flexible fibers in turbulent flows [30,31]. These chains provide a useful framework to understand the intricate interplay between elasticity and turbulent mixing [32–34] and provide insights which complement those obtained from other models with uniformly distributed mass [35,36], which are optimal for relatively more *rigid* fibers and well suited to studies of buckling, flapping, or as probes for two-point Eulerian statistics of the carrier flow. Here, we use the bead-spring chain model, which allows for a natural inclusion of elasticity, stiffness, and inertia to address issues of gravitational settling. In this context, the most striking feature of these filamentary chains is the manner in which they preferentially sample the geometry of a turbulent flow: In the absence of inertia and gravity, elastic chains preferentially sample the vortical regions of the flow, in both two and three dimensions (2D and 3D), though for different reasons [32,34]. This prediction, for the case of rigid chains in 3D, was recently confirmed experimentally [37]. The introduction of inertia (without gravity) counteracts this tendency due to centrifugal expulsion from vortices and decorrelation from the flow, resulting in rather distinct dynamics [33]. Here, we account for gravitational acceleration and investigate the settling dynamics of these *elastoinertial* chains. We mostly focus on the fully flexible limit, though we do show that our key results hold for stiff chains as well.

II. THE ELASTOINERTIAL CHAIN: A MINIMAL MODEL FOR FILAMENTS

We model a filament of mass M as a chain of N_b spherical beads. Considering ρ to be the mass density of the filament, we distribute the mass uniformly over the beads, each of radius $a \ll \eta$, so $\frac{4}{3}\pi a^3 \rho N_b = M$. The beads are then characterized by a Stokesian relaxation time $\tau_p = \frac{2\rho a^2}{9\rho_f \nu}$, where ρ_f and ν are the density and kinematic viscosity of the carrier fluid. Each bead, positioned instantaneously at $\mathbf{x}_j$, is connected to its nearest neighbors through (phantom) elastic links with which we associate a relaxation timescale τ_E (yielding an effective elastic timescale $\tau_E N_b(N_b+1)/6$ for the filament [32,38]), thus rendering our elastoinertial chains extensible (and fully flexible). The dynamics of these model filaments are then completely determined by the coupled equations of motion for the interbead separation vectors $\mathbf{r}_j = \mathbf{x}_{j+1} - \mathbf{x}_j$ and the center-of-mass $\mathbf{x}_c$:

$$\tau_p \ddot{\mathbf{r}}_j = [\mathbf{u}(\mathbf{x}_{j+1}, t) - \mathbf{u}(\mathbf{x}_j, t) - \dot{\mathbf{r}}_j] + A[\boldsymbol{\xi}_{j+1}(t) - \boldsymbol{\xi}_j(t)] + \frac{1}{4\tau_E}(f_{j-1}\mathbf{r}_{j-1} - 2f_j\mathbf{r}_j + f_{j+1}\mathbf{r}_{j+1}), \tag{1}$$

$$\tau_p \ddot{\mathbf{x}}_c = \left(\frac{1}{N_b}\sum_{j=1}^{N_b} \mathbf{u}(\mathbf{x}_j, t) - \dot{\mathbf{x}}_c\right) + \frac{A}{N_b}\sum_{j=1}^{N_b} \boldsymbol{\xi}_j(t) - \tau_p g\hat{\mathbf{z}}. \tag{2}$$

Here, we use the FENE (finitely extensible nonlinear elastic) interaction $f_j = (1 - |\mathbf{r}_j^2|/r_m^2)^{-1}$, with a prescribed maximum interbead length r_m, to model the springs. $\boldsymbol{\xi}_j(t)$ are independent white noises which, unlike in the case of polymers, do not represent Brownian forces but rather are introduced as a means to set the equilibrium length r_0 for each segment of our filament (in the absence of flow). The noise amplitude is chosen accordingly as $A^2 = \frac{r_0^2}{6\tau_E}$. The entire chain then has equilibrium and maximum end-to-end extensions of $R_0 = r_0\sqrt{N_b - 1}$ and $R_m = r_m(N_b - 1)$, respectively. We note that the precise method of enforcing the equilibrium length is not crucial to our study; in previous work, we omitted the noise and instead set the equilibrium length by using a spring force of $f_j(r_j - r_0)$, without affecting the qualitative dynamics of the chains in flow [34].

We choose a coordinate system such that the acceleration due to gravity g acts along the negative z axis. Finally, the timescales τ_p and τ_E, as well as the acceleration due to gravity g, allow us to define nondimensional numbers in terms of analogous (small-scale) quantities of the carrier turbulent flow, namely, the Kolomogorov time $\tau_\eta \equiv \sqrt{\nu/\epsilon}$ and acceleration $a_\eta \equiv (\epsilon^3/\nu)^{1/4}$, where ϵ is the mean energy dissipation rate of the flow. The dynamics of our filaments are thus completely determined by the Stokes number $\mathrm{St} \equiv \tau_p/\tau_\eta$ (a measure of the inertia), the Froude number $\mathrm{Fr} \equiv a_\eta/g$ (a measure of the force of gravity), and the Weissenberg number $\mathrm{Wi} \equiv \frac{N_b(N_b+1)\tau_E}{6\tau_\eta}$ (a measure of elasticity). Here, we have used the mapping proposed by Ref. [38] to estimate the effective relaxation time of the entire chain from τ_E (which corresponds to individual links).

Note that this model neglects the feedback of the chains onto the flow. Because we consider the extremely dilute limit of a single chain (we simulate many chains only to obtain good statistics), the motion of the chain does not affect the global flow. However, the chain will certainly modify the local flow field. This, in turn, would result in one portion of the chain influencing other portions via the disturbed flow. This effect can be accounted for within the bead-spring framework by including interbead hydrodynamic interactions (HIs), as has been done in polymer models [39,40]. However, the effect of HI on chain dynamics is minimal when the chain is stretched out by the flow. We therefore ignore HI for simplicity. Similarly, we also ignore excluded volume (EV) interactions. Bending stiffness is also disregarded for now, although we study its effect later in Sec. VI. Thus, our chain represents a minimal model of a filament, adopted to more clearly reveal the fundamental interplay between elasticity, inertia, and gravitational and turbulent acceleration.

It is also important to point out that other models of filament dynamics, particularly in the context of turbulent transport, are available [30,31,35,36]. However, studies for low Reynolds number flow [20] show that the bead-spring approach to filaments still remains an important framework [41–44] because of the limitations of models based on slender-body theory [45,46].

III. SIMULATIONS

In our direct numerical simulations of the turbulent carrier flow, we use a de-aliased pseudospectral algorithm and spatially discretize the 3D incompressible Navier-Stokes equations on a 2π periodic cubic box with $N^3 = 512^3$ collocation points. We use a second-order slaved Adams-Bashforth scheme for time integration [48]. The flow is driven to a statistically stationary state by using a constant energy injection scheme. We choose the coefficient of viscosity $\nu = 10^{-3}$ to obtain a Taylor-scale Reynolds number $\mathrm{Re}_\lambda \approx 200$. Filaments are introduced into the flow only after it attains stationarity. The fluid velocity $\mathbf{u}(\mathbf{x}, t)$, which is available on the regular periodic grid, is interpolated, using trilinear interpolation, to obtain the velocity $\mathbf{u}(\mathbf{x}_{j+1}, t)$ at the positions of the beads of each filamentary chain.

To evolve the chains, we use a second-order Runge-Kutta scheme for the deterministic terms of Eqs. (1) and (2), while the noise is treated using the Euler-Maruyama method [49]. (Such a combination of integration schemes has been used previously to study the Lagrangian dynamics of polymers in a turbulent flow [50].) Let us denote the time rate of change of the separation vectors $\mathbf{r}_j$ by $\mathbf{v}_j = d\mathbf{r}_j/dt$ ($j = 1, 2, ..N_b - 1$). Dropping the subscript j for ease of notation, Eq. (1) can be

written as

$$\frac{d\mathbf{r}}{dt} = \mathbf{v}, \quad \frac{d\mathbf{v}}{dt} = \frac{1}{\tau_p}[\mathbf{f}_{\text{spring}} + \mathbf{f}_{\text{noise}} + \mathbf{f}_{\text{drag}}],$$

where the various forcing terms are denoted by $\mathbf{f}$ with suitable subscripts. To evolve these equations from t to $t + \Delta t$, we begin by generating the random force $\mathbf{f}_{\text{noise}}$, and evaluating the deterministic force $\mathbf{f}_{\text{spring}} + \mathbf{f}_{\text{drag}}$ using the known values of $\mathbf{v}$ and $\mathbf{r}$ at time t. We then take a half step,

$$\mathbf{v}^h = \mathbf{v}(t) + \frac{1}{\tau_p}\left[\sqrt{\frac{\Delta t}{2}}\,\mathbf{f}_{\text{noise}} + \frac{\Delta t}{2}\,(\mathbf{f}_{\text{spring}} + \mathbf{f}_{\text{drag}})\right],$$

$$\mathbf{r}^h = \mathbf{r}(t) + \frac{\Delta t}{2}\mathbf{v}^h,$$

where $\mathbf{v}^h$ and $\mathbf{r}^h$ are the values of the corresponding variables at the midpoint $t + \Delta t/2$. These midpoint values are used to update the deterministic force, yielding $\mathbf{f}^h_{\text{spring}} + \mathbf{f}^h_{\text{drag}}$, where the calculation of the drag force requires updating the positions of the beads, followed by interpolating the fluid velocity at the beads. The additive noise $\mathbf{f}_{\text{noise}}$ remains unchanged over the interval Δt. We then take a full step to advance $\mathbf{v}$ and $\mathbf{r}$ to $t + \Delta t$:

$$\mathbf{v}(t + \Delta t) = \mathbf{v}(t) + \frac{1}{\tau_p}\left[\sqrt{\Delta t}\,\mathbf{f}_{\text{noise}} + \Delta t\,\left(\mathbf{f}^h_{\text{spring}} + \mathbf{f}^h_{\text{drag}}\right)\right],$$

$$\mathbf{r}(t + \Delta t) = \mathbf{r}(t) + \mathbf{v}^h \Delta t.$$

Equation (2) for the center of mass is integrated in a similar fashion. The equations for the filaments are solved simultaneously with the Navier-Stokes equations. The time steps used for the flow Δt_f and for the chains Δt_c are the same, except for the simulations with bending stiffness, described below in Sec, VI, where $\Delta t_c/\Delta t_f$ has to be decreased down to $1/70$ for the stiffest chain.

We evolve an ensemble of 10^4 filaments, each with an equilibrium end-to-end extension of $R_0 = 15.6\eta$, a maximum length $R_m = 270\eta$, and $N_b = 10$ beads (we have checked that our results remain qualitatively unchanged if we use a fewer number of beads, $N_b = 5$), and consider $0.1 \leqslant \text{St} \leqslant 8.0$, $0.5 \leqslant \text{Wi} \leqslant 40$, and $0.5 \leqslant \text{Fr} \leqslant 2.0$. A visualization of a few chains settling through the turbulent flow is presented in Fig. 1 where we identify the vortex tubes using the Q criterion [47].

IV. FLUCTUATING SETTLING VELOCITY

We begin our study by examining the fluctuating settling velocities $v_z \equiv \dot{\mathbf{x}}_c \cdot \hat{\mathbf{z}}$ of the filaments. Let us first consider the mean value $\langle v_z \rangle$, where the angular brackets denote an average over the ensemble of chains and over time in the statistically stationary state. From Eq. (2), denoting $a_z \equiv \ddot{\mathbf{x}}_c \cdot \hat{\mathbf{z}}$ as the vertical acceleration in the z direction, the assumption of a mean settling velocity implies, by definition, that $\langle a_z \rangle = 0$. Furthermore, since the noises are independent and of zero mean, we obtain $\langle v_z \rangle = \langle \bar{u}_z \rangle - \tau_p g$, where $\tau_p g$ is the terminal settling velocity in a still fluid, and $\bar{u}_z \equiv \frac{1}{N_b}\sum_{j=1}^{N_b} u_z(\mathbf{x}_j, t)$ is the average z component of the fluid velocity field sampled by the filament. If an object uniformly samples the flow, as tracer particles do, then $\langle \bar{u}_z \rangle = 0$. However, this is typically not the case for nontracers: Heavy inertial particles (with $\text{St} > 0$) are known to exhibit an enhanced mean settling velocity. The magnitude of this effect, which may be quantified through $\Delta_V = -(\langle v_z \rangle/\tau_p g + 1) = -\langle \bar{u}_z \rangle/\tau_p g$, varies nonmonotonically with St as explained in Ref. [7].

Now, as instantiated by our model, a filament can be thought of as a string of elastically linked, inertial particles. So, how does this internal linking impact the mean settling velocity of filaments? Figure 2(a) answers this question by presenting simulation results of Δ_V as a function of St for filaments with $\text{Fr} = 2$ (results for $\text{Fr} = 1$ and 0.5 are qualitatively similar but with reduced magnitudes of Δ_V) and various values of Wi, as well as for free inertial particles [whose dynamics

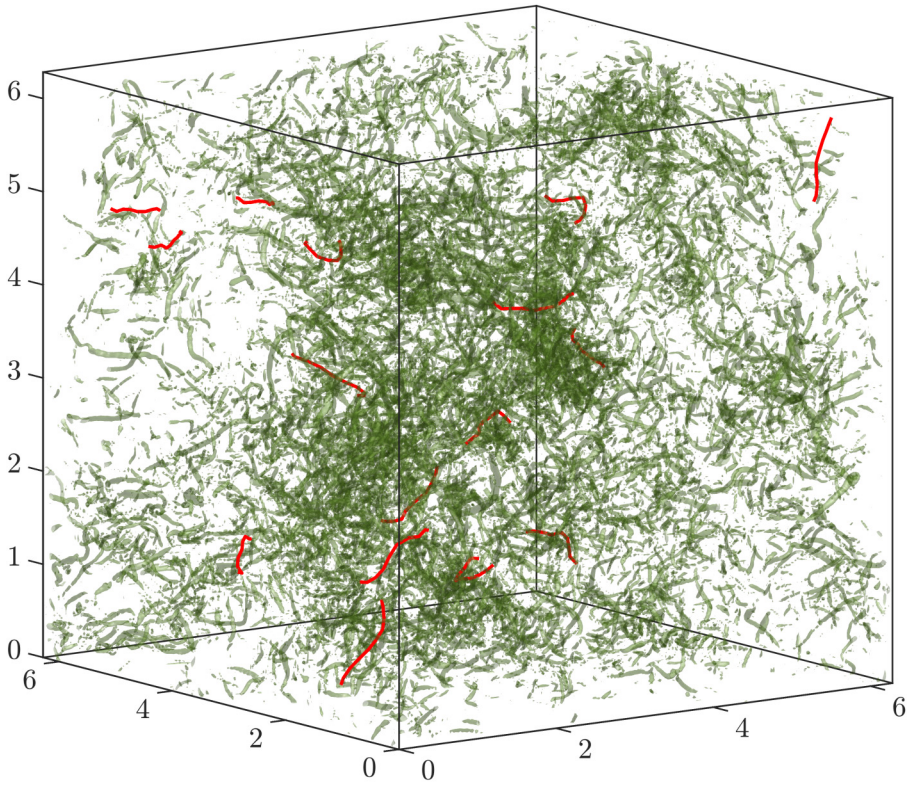

FIG. 1. Representative snapshot of a few elastic filaments (red curves) sedimenting through a turbulent flow. The intense vortex tubes (green contours) of the flow are visualized via isosurfaces of the $\mathcal{Q}$ field $(3\langle\mathcal{Q}^2\rangle^{-1/2})$ [47]. The parameters of the filaments are Wi $= 20$, St $= 2$, and Fr $= 1$.

are given by Eq. (2) with $A = 0$ and $N_b = 1$]. Comparing the results for particles and filaments, we see that the elastic links reduce the level of enhancement, but only up to moderate values of St. At large St, the results for chains approach that for free particles.

Let us first consider the case of small to moderate St, for which the enhanced settling velocity of particles is due to a preferential sampling of the downward-flowing regions of the flow (i.e., on average, the z component of the fluid velocity sampled by the particles is negative, $\langle\bar{u}_z\rangle < 0$, and not zero as it would be for tracers) [7]. When these same particles are linked together to form long chains, they can no longer remain inside these regions of the flow. The chains in our work have inertial-scale lengths that increase with Wi as the chains are stretched out by the flow, as depicted in Fig. 2(b), which shows the probability distribution function (PDF) of the end-to-end extension $R \equiv |\sum_{j=1}^{N_b-1} \mathbf{r}_j|$. At Wi $= 0.5$, the chains are mostly at the equilibrium extension, while at Wi $= 40$ they are broadly distributed with several near the maximum length. Despite this variation in extension, the value of Δ_V barely changes with Wi. This tells us that even the equilibrium size of approximately 15η is too large for the chains to preferentially sample the down-welling zones of the flow. Further increase in the extension with Wi, thus, has no additional effect on the mean settling velocity.

Turning to the case of large St, we note that both particles and chains decorrelate from the underlying flow when St $\gg 1$. So, preferential sampling is no longer important, and the particles or chains experience the flow as a short-correlated noise [7]. Moreover, at large St, the effect of elasticity weakens relative to that of inertia, so the chains begin to settle, on average, like a collections of free beads. Thus, we see in Fig. 2(a) that Δ_V for the chains approaches the result

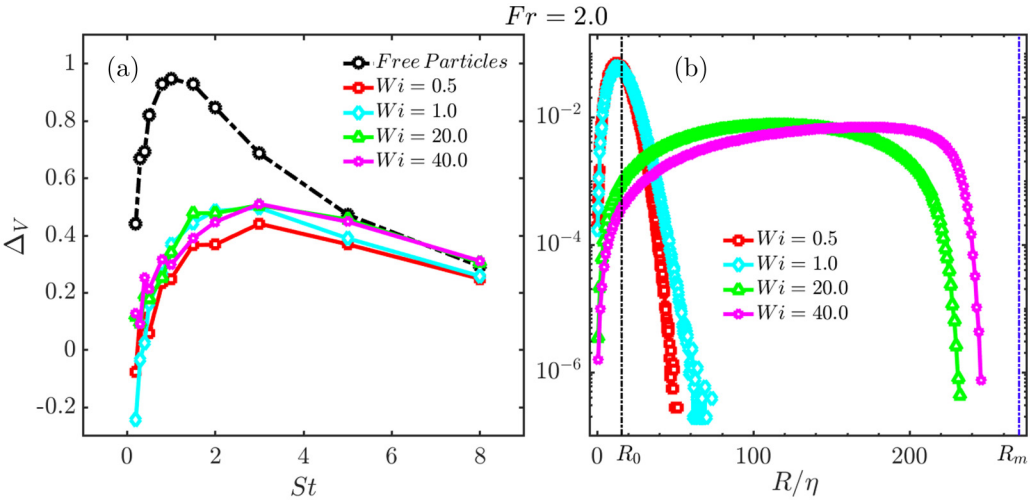

FIG. 2. (a) Plot of the relative enhancement in the mean settling velocity Δ_V, over the still fluid value, as a function of St, for free, inertial, point particles, and for filaments with different values of Wi. (b) Probability distribution function of the end-to-end extension of the filament for the same values of Wi as in (a). The equilibrium and maximum lengths for all filaments are $R_0 = 15.6\eta$ (dashed black line) and $R_m = 270\eta$ (dashed blue line) respectively. In both panels, Fr $= 2$.

for free particles as St increases, with the values for larger Wi chains (weaker elastic forces) being closer to the free particle limit.

Next, let us examine how the settling velocity fluctuates about its mean value. The PDF of v_z, illustrated in the inset of Fig. 3, shows that the turbulent flow can produce strong temporal fluctuations—much greater than Δ_V—which become increasingly large and slightly non-Gaussian (the black lines are Gaussian fits) as St/Fr increases (the relevance of this ratio becomes clear below). The magnitude of these fluctuations is best quantified through the normalized variance $\sigma \equiv \frac{\langle v_z^2\rangle}{\langle v_z\rangle^2} - 1$ of the distribution. To obtain a theoretical estimate for this variance, we use Eq. (2) to calculate the second moment of the settling velocity $\langle v_z^2\rangle$. Noting that $\sum_{j=1}^{N_b}\sum_{k=1}^{N_b}\langle \xi_{j,z}(t)\xi_{k,z}(t')\rangle = C\delta_{j,k}\delta(t-t')$, where the subscript z denotes the z components of the noise and C is a constant (which absorbs the N_b factor) with the dimension of inverse time, we obtain $\langle v_z^2\rangle = \langle \bar{u}_z^2\rangle + \tau_p^2 g^2 + \tau_p^2\langle a_z^2\rangle + CA^2$, which on using $\Delta_V < 1$ leads to the nondimensional, normalized variance:

$$\sigma \approx \left[\frac{\langle \bar{u}_z^2\rangle + CA^2}{(a_\eta \tau_\eta)^2} + \mathrm{St}^2\frac{\langle a_z^2\rangle}{a_\eta^2}\right]\left(\frac{\mathrm{St}}{\mathrm{Fr}}\right)^{-2}. \tag{3}$$

This result is further simplified by the observation, from our simulations, that $\langle \bar{u}_z^2\rangle \approx (3/2)E$, where E is the mean kinetic energy of the flow. This leads to $\frac{\langle \bar{u}_z^2\rangle}{(a_\eta\tau_\eta)^2} \sim \sqrt{\mathrm{Re}}$, where Re is the large scale Reynolds number. Furthermore, we anticipate that, for finite Fr, $St^2\frac{\langle a_z^2\rangle}{a_\eta^2} \ll \sqrt{\mathrm{Re}}$ for all St, because for St $\ll 1$, $\langle a_z^2\rangle \sim a_\eta^2$ (chains follow the flow), while for St $\gg 1$, $\langle a_z^2\rangle \ll a_\eta^2$ (chains fall with their terminal velocity), and in both cases this term becomes negligibly small. Indeed, we have found from our numerical data that the term $\mathrm{St}^2\frac{\langle a_z^2\rangle}{a_\eta^2}$ is at least one order of magnitude smaller than $\frac{\langle \bar{u}_z^2\rangle}{(a_\eta\tau_\eta)^2}$ for all Wi and the ranges of St and Fr that we consider. Finally, the additive contribution of the noise, $CA^2 \propto 1/\mathrm{Wi}$, may also be neglected as it is small compared to the variance induced by

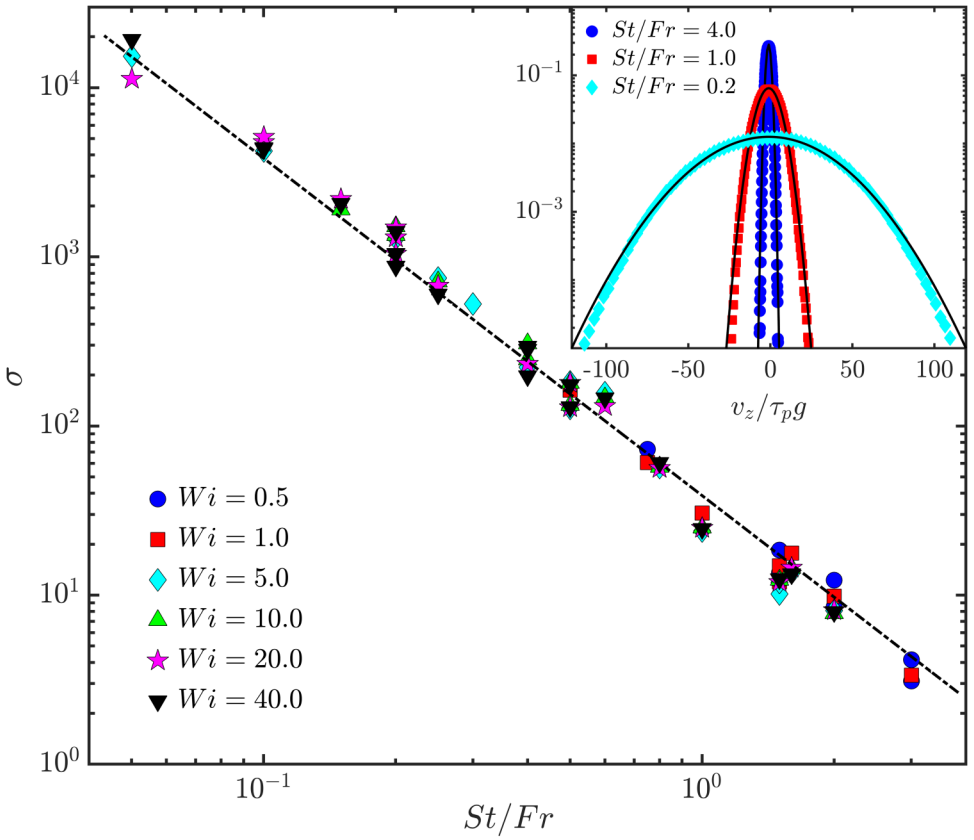

FIG. 3. Log-log plot of the normalized variance σ as a function of St/Fr; the different symbols correspond to different values of Wi (see legend) with the thick, black dashed line showing $(\mathrm{St/Fr})^{-2}$. Inset: Representative plots of the PDFs (from which σ is extracted) of the settling speed v_z rescaled by the corresponding $\tau_p g$ for $\mathrm{Wi} = 40$ and different values of St/Fr; the black lines are Gaussian fits.

the turbulent flow. Moreover, as mentioned earlier, the noise has no physical significance other than serving as a means to maintain the equilibrium length r_0 in a still fluid.

It follows, therefore, that to leading order $\sigma \sim (\mathrm{St/Fr})^{-2}$; the variance only depends on a single *settling parameter*$\mathrm{Sv} = \mathrm{St/Fr}$, which is the ratio of the still-fluid terminal settling velocity $\tau_p g$ to the Kolmogorov-scale velocity of the turbulent flow $u_\eta = a_\eta \tau_\eta$ [51].

Motivated by this scaling result, we plot the value of σ obtained from our simulations, carried out by varying Wi, St, and Fr *independently* over a range of values, against St/Fr in Fig. 3. We see that the leading order behavior of the variance matches the scaling prediction $\sigma \sim (\mathrm{St/Fr})^{-2}$ (dotted line) to a good approximation (see Fig. 3), over a wide range of Wi. Clearly, the extent of elasticity and therefore the stretching of the filament does not appreciably impact the settling velocity statistics.

V. TUMBLING: A POISSON PROCESS

So far, we have only considered the settling of the filament as a whole. However, unlike for instance spherical particles, these filaments have additional internal degrees of freedom which raise new questions, of which perhaps the most interesting is to understand how the filaments tumble as they descend through the turbulent flow. It is useful to recall that the tumbling of individual

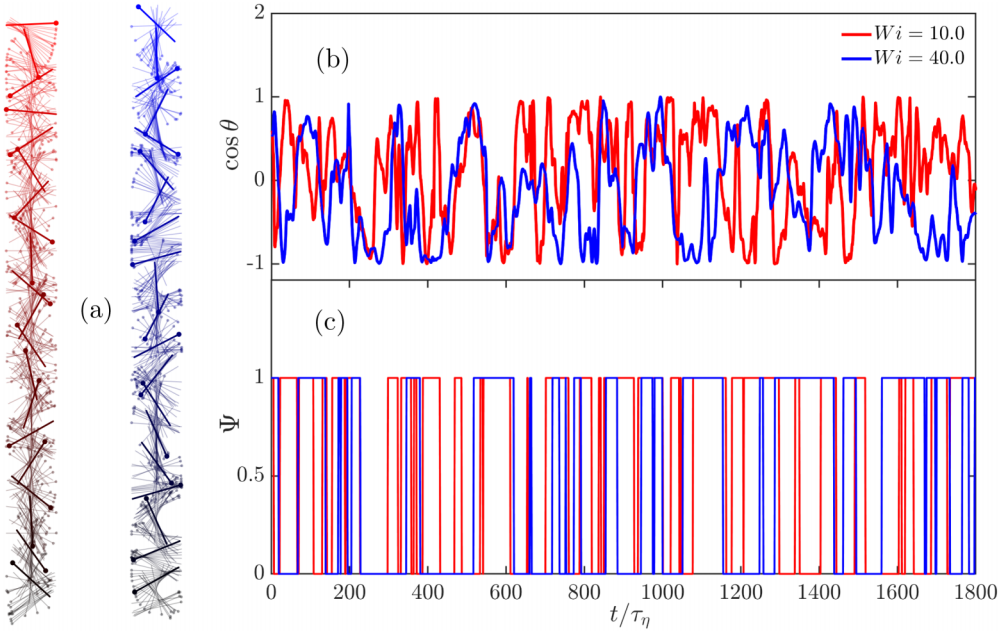

FIG. 4. (a) Representative time trace of snapshots of the end-to-end vectors $\mathbf{R}$ of two filaments with Wi = 10 (red) and 40 (blue) at different times (increasing downward) as they sediment (St = 2, Fr = 0.5); the vectors are projected on a 2D plane to illustrate the change in orientation θ with respect to the direction of gravity $-\hat{\mathbf{z}}$. The filaments have been shown in intervals of $3.5\tau_\eta$ and the ones in bolder colors at $68\tau_\eta$. Plots of (b) $\cos\theta$ and (c) Ψ (see text) of the same filaments as a function of nondimensional (with τ_η) time: $\Psi = 1(0)$ corresponds to an up (down) state of our filaments.

polymers—small elastic chains unaffected by inertia or gravity—has been studied in the context of simple shear flows [52,53].

To study tumbling quantitatively, we consider the dynamics of the end-to-end vector $\mathbf{R} \equiv \sum_{j=1}^{N_b-1} \mathbf{r}_j$. In Fig. 4(a), we show typical time traces of the end-to-end vector projected on a two-dimensional plane for two sedimenting filaments with different Wi (and St = 2, Fr = 0.5). Clearly, the filaments undergo complicated *rotational* dynamics accompanied by tumbling events. This behavior is quantified through the cosine of the angle made by $\mathbf{R}$ with the z axis via $\mathbf{R} \cdot \hat{\mathbf{z}} = R\cos\theta$, where $R = |\mathbf{R}|$. In Fig. 4(b), we show plots of the time series of $\cos\theta$ for the two filaments shown in Fig. 4(a). This time series illustrates the seemingly continuous changes in the orientation of the settling filaments with a suggestion that filaments tumble more frequently as the Wi decreases. Such observations naturally lead us to (i) suitably define the *state* Ψ of the filament as being either "up" or "down" and (ii) to characterize the transitions between these two states.

We define the up and down states as $\Psi = 1$ for $\cos\theta \geqslant 0$ and $\Psi = 0$ for $\cos\theta < 0$, respectively. The apparently random switching between the two states, clearly illustrated in Fig. 4(c), is quantified by calculating the PDFs $P^+(\tau)$ ($P^-(\tau)$) of the residence time τ over which the filaments remain up (down). These distributions yield the probability of a filament in an up (or down) state to continue to remain in the same state for a duration of τ. We recall that questions of this sort—the so-called persistence problems—have a special importance in areas of non-equilibrium statistical physics [54–57] and, more recently, have been adapted to understand the geometrical aspects of turbulent flows [58–60].

In Fig. 5(a), we show semilog plots of $P^+(\tau)$ for filaments with St = 2.0, Fr = 0.5, but different degrees of elasticity. We have confirmed, by varying the range of angles θ which define an up or down state, that the precise definition of these states does not affect the results qualitatively;

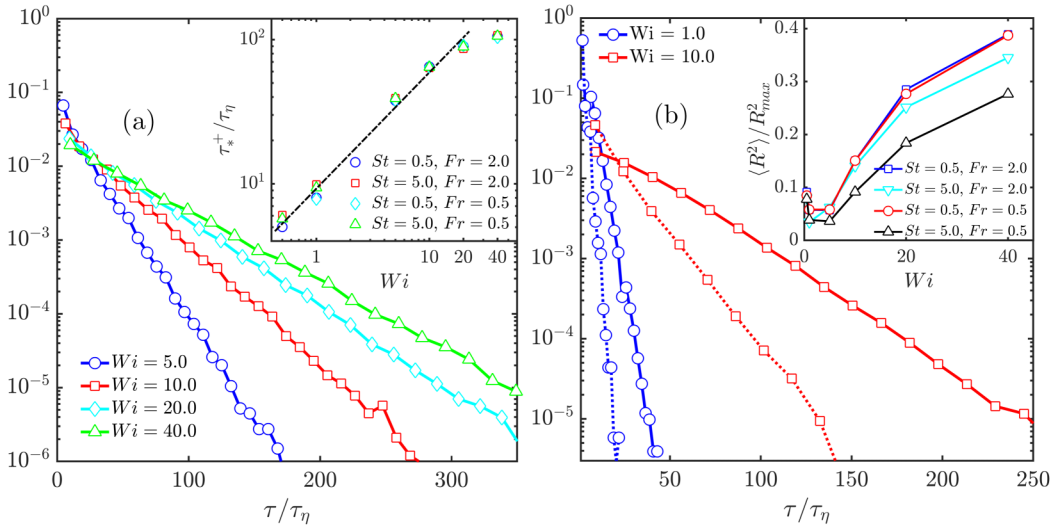

FIG. 5. (a) Probability distribution functions $P^+(\tau)$ of the residence time in the up ($\Psi = 1$) state for filaments with St = 2.0, Fr = 0.5, and different values of Wi. Inset: Log-log plot of the characteristic timescale τ_*^+ versus Wi for different values of St and Fr; the thick black line indicates a scaling of $\mathrm{Wi}^{4/5}$. (b) Conditioned probability distribution functions of time spent in the up ($\Psi = 1$) state, for filaments with relatively small ($\langle R \rangle_+ < \ell_1$; dashed lines) and large ($\langle R \rangle_+ > \ell_2$; solid lines) time-averaged lengths. The values of the thresholds for the two cases are $\ell_1 = 9\eta$, $\ell_2 = 20\eta$ for Wi = 1, and $\ell_1 = 40\eta$, $\ell_2 = 65\eta$ for Wi = 10. In both cases, St = Fr = 1.0. Inset: Plot of normalized $\langle R^2 \rangle$, versus Wi for different values of St and Fr.

furthermore, $P^+(\tau) = P^-(\tau)$ because the problem is symmetric to the transformation $r_j \to -r_j$ which reverses the end-to-end vector. These distributions clearly show an exponential fall-off: $P^+(\tau) \sim \exp(-\tau/\tau_*^+)$, which indicates that tumbling manifests as a Poisson process (which also characterizes, for example, the escape of particles from vortices [60] and the turbulent entrainment of coarse grains [61]). The characteristic timescale τ_*^+ ($= \tau_*^-$) has a weak dependence on St and Fr, but increases systematically with Wi (see Ref. [53] for single polymers in a shear flow), as seen in the inset of Fig. 5(a).

Why do more extensible filaments require longer times to tumble? The answer lies in the connection between the dynamic length of a filament and its tumbling. We expect a highly stretched, long filament that spans multiple flow eddies to have a lower probability of experiencing the sequence of coordinated drag forces required to cause a transition in its orientation. To test this hypothesis, we calculate the average end-to-end length of a filament over each interval of time spent in the up state $\langle R \rangle_+$. When a transition occurs, we record $\langle R \rangle_+$ along with the persistence time τ, which then allows us to obtain the PDF of τ conditioned on the time-averaged length of the filament. Figure 5(b) shows these conditioned PDFs for relatively short (dashed line) and long (solid line) filaments, defined as those with $\langle R \rangle_+ < \ell_1$ and $\langle R \rangle_+ > \ell_2$ ($\ell_1 < \ell_2$), where the values of the thresholds depend on Wi and are given in the figure caption (small variations in these values do not affect our conclusions). Two values of Wi are considered, and in both cases we see that when filaments are more stretched they do indeed take a longer time to tumble. Now, as Wi increases, the filaments become more extensible and the distribution of R broadens. This is demonstrated by the inset of Fig. 5(b), which presents the variation of $\langle R^2 \rangle$ with Wi. As a result, a larger Wi filament is much more likely to be in a highly stretched state, which explains its tendency to persist in a given orientation for a longer time before tumbling. The consequent increase of τ_*^+ with Wi, shown in the inset of Fig. 5(a), appears to follow a power law (the fitted dashed line has an exponent of 4/5)

for small to moderate Wi, but then begins to level off at large Wi, as the filament approaches its maximum length.

Interestingly the tumbling time τ_*^+ is seen to be almost independent of Fr. In fact, we have checked, by running additional simulations, that neutrally buoyant chains (Fr $= \infty$) exhibit the same power-law dependence of τ_*^+ on Wi as that seen in the inset of Fig. 5(a). This result is closely related to a recent experimental observation made by Oehmke *et al.* [37] for rigid, inextensible, neutrally bouyant fibers in isotropic turbulence. They find that the variance of the tumbling rate decreases with the (fixed) length L of the fiber as a power law, $L^{-4/3}$, which can be derived by assuming that the tumbling rate is determined by the inverse of the turnover time of an inertial range eddy of scale L [37]. In our case of extensible fibers, the situation is more complex, as we have a dynamically varying filament length, with a broad distribution that widens with Wi [cf. Fig. 2(b) and the inset of Fig. 5(b)].

VI. STIFF CHAINS

How valid are our results when the filaments are *stiff*? Chains with bending stiffness have an energy cost associated with bending, which manifests as an additional force on the beads of the chain. The bending energy is defined using the angles (via the dot product) between successive link vectors, such that a relatively inflexible filament has a larger bending cost and so is more likely to remain in a rodlike configuration. If S is the measure of bending stiffness, then the resulting force acting on the jth bead is given as [62]

$$\boldsymbol{f}_j^B = \frac{S}{r_0}\Bigg[\frac{\alpha_{j-2}}{r_{j-1}}\hat{\boldsymbol{r}}_{j-2} - \left(\frac{\alpha_{j-2}}{r_{j-1}}\hat{\boldsymbol{r}}_{j-2}\cdot\hat{\boldsymbol{r}}_{j-1} + \frac{\alpha_{j-1}}{r_j} + \frac{\alpha_{j-1}}{r_{j-1}}\hat{\boldsymbol{r}}_{j-1}\cdot\hat{\boldsymbol{r}}_j\right)\hat{\boldsymbol{r}}_{j-1} \tag{4}$$

$$+\left(\frac{\alpha_{j-1}}{r_j}\hat{\boldsymbol{r}}_{j-1}\cdot\hat{\boldsymbol{r}}_j + \frac{\alpha_{j-1}}{r_{j-1}} + \frac{\alpha_j}{r_j}\hat{\boldsymbol{r}}_j\cdot\hat{\boldsymbol{r}}_{j+1}\right)\hat{\boldsymbol{r}}_j - \frac{\alpha_j}{r_j}\hat{\boldsymbol{r}}_{j+1}\Bigg], \tag{5}$$

with

$$\alpha_j = \begin{cases} 0 & \text{if } j \leqslant 0 \text{ or } j = N_b \\ 1 & \text{otherwise.} \end{cases} \tag{6}$$

The characteristic time associated with the bending force is $\tau_B = \zeta r_0^3/S$, where ζ is the Stokes drag on the beads and r_0 is the equilibrium length of the elastic links. Similar to the Weissenberg number, we define a dimensionless measure of bending stiffness as the bending Weissenberg number $\mathrm{Wi}_B = \tau_B/\tau_\eta$. The filaments become inflexible for small Wi_B, while the limit of fully flexible filaments is attained for large Wi_B.

The equation of motion for the links [Eq. (1)] now includes the additional term $\frac{1}{\zeta}(\boldsymbol{f}_{j+1}^B - \boldsymbol{f}_j^B)$ on the right-hand side to account for bending stiffness. However, because these bending forces are internal to the filaments, they do not affect the motion of the center of mass explicitly and so its equation of motion remains identical to that of fully flexible filaments [Eq. (2)].

We now simulate these filaments in a turbulent flow using the techniques described in Sec. III; however, these additional simulations were performed on a smaller $N^3 = 256^3$ grid and consequently with a smaller Taylor-scale based Reynolds number $\mathrm{Re}_\lambda \approx 111$. Furthermore, we use a wide range of the bending Weissenber number $1.6 \times 10^{-3} < \mathrm{Wi}_B < 1.6 \times 10^3$, along with $0.16 < \mathrm{St} < 12.72$, $0.8 < \mathrm{Wi} < 64$ and $0.5 < \mathrm{Fr} < 2$.

To see how the addition of bending stiffness straightens out the chains, let us examine the angle between successive link vectors, averaged over all hinges of the chain, defined as

$$\overline{\phi} \equiv \frac{1}{N_b - 2}\sum_{j=1}^{N_b-2}\cos^{-1}(\hat{t}_j\cdot\hat{t}_{j+1}), \quad \text{where } \hat{t}_j = \mathbf{r}_j/|\mathbf{r}_j|. \tag{7}$$

A perfectly straight chain would have $\overline{\phi} = 0$.

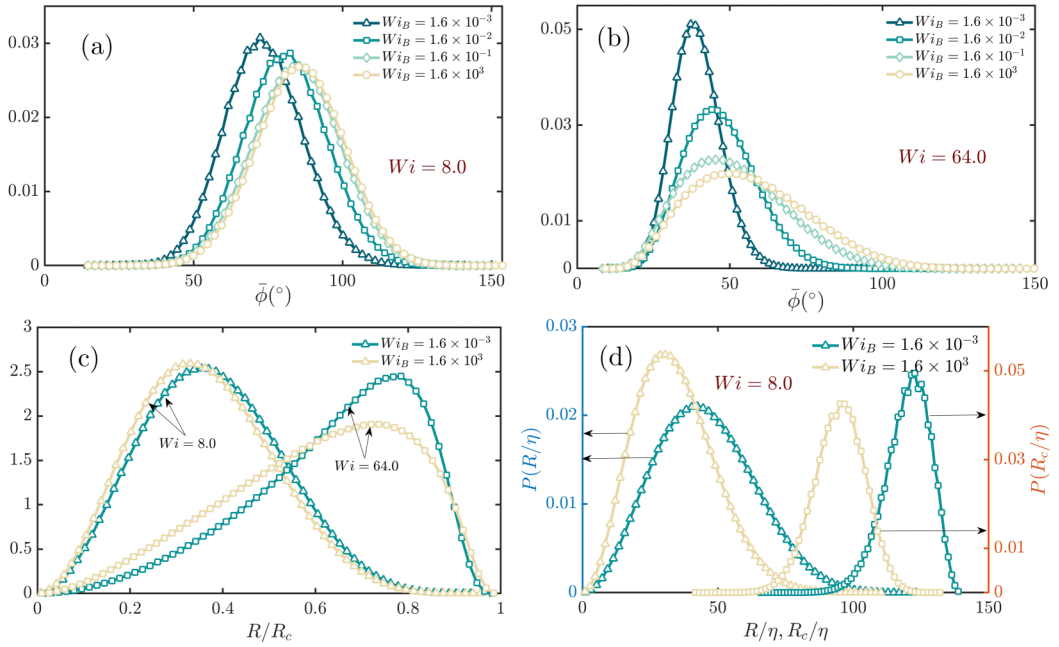

FIG. 6. (a) Probability distribution function (PDF) of the mean angle between successive links of a chain $\overline{\phi}$, for different extents of bending stiffness (Wi_B) and for $\mathrm{Wi} = 8$. (b) Same as panel (a) but for $\mathrm{Wi} = 64$. (c) PDF of the ratio of the end-to-end extension to the contour length of the chain (R/R_c), for $\mathrm{Wi} = 8$ and 64, and for two contrasting values of Wi_B. (d) PDF of the end-to-end extension (left axis) and the contour length (right axis), normalized by the Kolmogorov length, for $\mathrm{Wi} = 8$ and two contrasting values of Wi_B. All plots correspond to $\mathrm{Fr} = 1.0$.

Figure 6(a) presents the PDF of $\overline{\phi}$ for $\mathrm{Wi} = 8$ and four different values of the nondimensional bending timescale Wi_B, ranging in magnitude from 10^3 (indistinguishable from a fully flexible chain) to 10^{-3}. The distribution is clearly seen to shift toward smaller angles, indicating that the chain straightens out as the bending stiffness is increased (Wi_B is decreased). This effect is more dramatic at higher Wi as seen in Fig. 6(b). Both these plots correspond to $\mathrm{Fr} = 1.0$, and are representative of the results for other values of Fr as well.

Next, consider the ratio of the end-to-end extension R to the contour length of the chain $R_c \equiv \sum_{j=1}^{N_b-1} |\mathbf{r}_j|$, which should be unity for a perfectly straight chain. PDFs of R/R_c are presented in Fig. 6(c). Here, the two different colors correspond to results for a highly flexible chain and a stiff chain. A comparison shows, surprisingly, that the shift in the peak of the PDF toward unity is very mild. This is true for both $\mathrm{Wi} = 8$ and 64. The reason for this is revealed by Fig. 6(d), which shows the effect of Wi_B on the PDFs of R and R_c separately. We see that stiffer chains are more easily stretched by the flow so R_c increases substantially with decreasing Wi_B, even as R increases. Thus, although the ratio R/R_c would approach unity in the rigid-rod limit, it is not an effective measure of the straightness of a *moderately stiff* extensible filament; of course, this ratio would work well for an inextensible filament.

How does the settling statistics of stiff, relatively straight chains compare with that of full-flexible ones? Figure 7(a) shows a log-log plot of the normalized variance σ versus the settling parameter $\mathrm{Sv} = \mathrm{St}/\mathrm{Fr}$ for a wide range of Wi_B. Clearly, the addition of the bending stiffness does not alter the scaling form $\sigma \sim (\mathrm{St}/\mathrm{Fr})^{-2}$ (indicated by the thick black line), obtained earlier for fully flexible filaments. This is not surprising because the theoretical derivation of the scaling for σ, to leading order, is insensitive to Wi_B. Furthermore, in the inset of Fig. 7(a) we show a plot of the settling

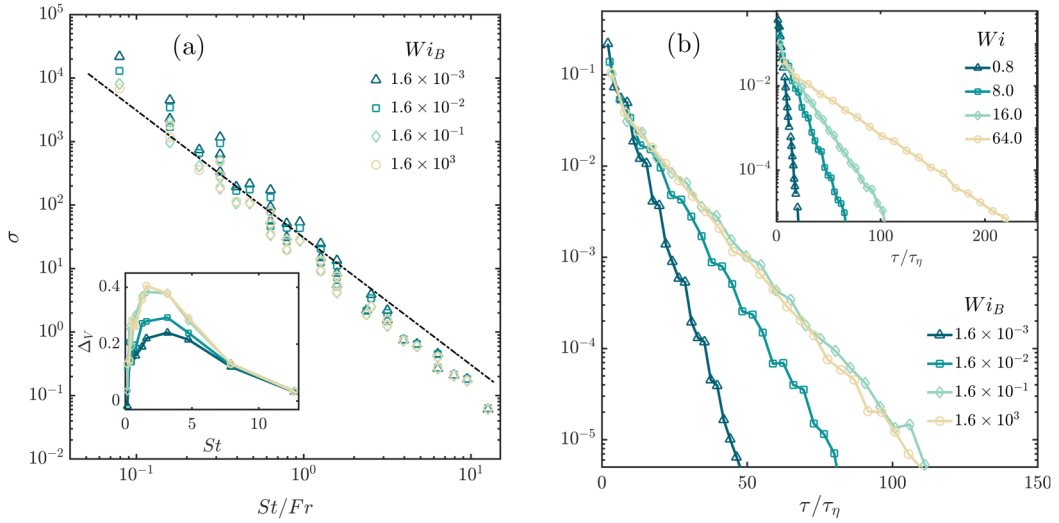

FIG. 7. (a) Log-log plot of the normalized variance σ versus the settling parameter St/Fr for different values of Wi_B; the thick black line is a guide to the eye indicating a scaling form of $(\mathrm{St/Fr})^{-2}$. In the inset, we show a representative plot of Δ_V vs St for Fr = 2.0 and Wi = 16.0 and different values of Wi_B. (b) Semilog plots of $P^+(\tau)$ for filaments with Fr = 1.0, St = 1.26, and Wi = 16.0 and different values of Wi_B; in the inset, we plot the same distributions for stiff ($\mathrm{Wi}_B = 1.6$) filaments with the same Stokes and Froude numbers but varying Wi.

velocity Δ_V, for different values of Wi_B, which shows the same nonmonotonic behavior with St as seen in Fig. 2 for fully flexible chains. However, as Wi_B is decreased, the degree of enhancement of the settling velocity reduces from the value for fully flexible chains. So, stiffness acts along with elasticity to constrain the motion of the filament and prevent it from preferentially sampling downward moving regions of the flow.

Next, consider the effect of bending stiffness on tumbling. Two counteracting effects come to mind. One the one hand, stiff chains have greater end-to-end extensions [Fig. 6(d)], and as more extended chains take longer to tumble [Fig. 5(b)], we may expect stiff chains to tumbler slower than flexible ones. On the other hand, it is easier for the fluctuating drag to flip a stiff chain that is constrained to remain relatively straight, as compared to a fully flexible chain. Our data shows that the second effect wins out. Figure 7(b) presents representative plots of the distribution $P^+(\tau)$ of residence times τ for which filaments persist in the up orientation, for different values of Wi_B, with Fr = 1.0, St = 1.26, and Wi = 16.0 (the inset shows how, for a given $\mathrm{Wi}_B = 1.6$, Fr = 1.0 and St = 1.26, these exponential distributions vary with changing Wi). The characteristic tumbling time is seen to be lesser for smaller Wi_B, clearly demonstrating that stiffer chains tumble faster.

Overall, the results presented here for stiff chains confirm that the central conclusions drawn from studying fully flexible filaments are unchanged even with the inclusion of bending stiffness. We note that this is consistent with a recent study [34] that showed that the qualitative aspects of the preferential sampling of 3D turbulent flows by filaments are unchanged when bending stiffness is included to make such chains more inflexible.

VII. CONCLUDING REMARKS

To summarize, we have analyzed two complementary aspects of the dynamics of long and heavy, elastic filaments in a turbulent flow: the fluctuating settling velocity, and the transitions in vertical orientation associated with tumbling. For a given turbulent flow, we have found, rather surprisingly, that to leading order the weight of the filament only impacts its settling velocity [via the

St dependence of Δ_V and the $(\mathrm{St}/\mathrm{Fr})^{-2}$ scaling of σ] while the elasticity and consequent stretching of the filament only affects its tumbling. Furthermore, we perform additional simulations for chains with a bending energy and have found that our central results remain qualitatively unchanged, although stiff filaments settle slower but tumble faster than fully-flexible ones.

The influence of stiffness on tumbling is actually subtle. As pointed out in the previous section, there are (at least) two competing effects at play. While in our simulations it is true that the one which allows a faster flipping dominates, the possibility of stiffer chains tumbling slower is not entirely inconceivable, especially for lower Reynolds number flows wherein the fluid drag acts more coherently across the filament. We indeed find some evidence of this in simulations at lower Reynolds numbers. However, this issue requires a further focused investigation, in a simpler system shorn of the complexities of the present problem.

In our simulations, we have neglected EV and HIs between different portions of the filament, i.e., between different beads of the chain. While these interactions are unimportant at large values of Wi when the chain is strongly stretched out by the flow, they will be significant for filaments with $\mathrm{Wi} \lesssim 1$. It is left as a task for future work to include HI and EV forces and study the behavior of weakly stretched filaments in more detail. Including these intrafilament interactions would also be important for studying the scaling relationships of the settling and tumbling characteristics of the filament as a function of its length (by systematically increasing the number of beads).

The Poisson distribution of tumbling times brings to mind the Poissonian *back-and-forth* motion of filamentary, motile microorganisms. Such a tumblinglike motion is thought to be an efficient strategy for foraging [26,27], but given that the Reynolds number of oceanic turbulence [28] is similar to that in our paper, it is tempting to consider in future work whether the tumbling of marine filamentary microorganisms are a consequence of active strategy or physical inevitability. Admittedly, these microorganisms are motile and much smaller than our filaments; nevertheless, our results should motivate work on longer marine organisms and their journey as they settle in the ocean.

ACKNOWLEDGMENTS

We are grateful to Dario Vincenzi for many insightful discussions and for introducing us to this problem. R.K.S. and S.S.R. also thank A. Kundu for useful discussions. We are also grateful to Siddhartha Mukherjee for his help in visualizing the falling filaments. The simulations were performed on the ICTS clusters *Contra* and *Tetris* as well as the work stations from Project No. ECR/2015/000361: *Goopy* and *Bagha*. S.S.R. and R.K.S. acknowledge support of the DAE, Govt. of India, under Project No. 12-R&D-TFR-5.10-1100 and SSR SERB-DST (India) Projects No. MTR/2019/001553, No. STR/2021/000023, and No. CRG/2021/002766 for financial support. S.S.R. would like to thank the Isaac Newton Institute for Mathematical Sciences for support and hospitality during the program Mathematical Aspects of Turbulence: Where Do We Stand? (EPSRC Grant No. EP/R014604/1) when part of this work was done. J.R.P. gratefully acknowledges support received as a Faculty Associate of the International Centre for Theoretical Sciences, and is thankful for funding from the IIT-Bombay IRCC Seed Grant and SERB-DST (India) Project No. SRG/2021/001185.

[1] M. Maxey, The gravitational settling of aerosol particles in homogeneous turbulence and random flow fields, J. Fluid Mech. **174**, 441 (1987).

[2] L.-P. Wang and M. Maxey, Settling velocity and concentration distribution of heavy particles in homogeneous isotropic turbulence, J. Fluid Mech. **256**, 27 (1993).

[3] A. Aliseda, A. Cartellier, F. Hainaux, and J. C. Lasheras, Effect of preferential concentration on the settling velocity of heavy particles in homogeneous isotropic turbulence, J. Fluid Mech. **468**, 77 (2002).

[4] S. Ghosh, J. Dávila, J. Hunt, A. Srdic, H. Fernando, and P. Jonas, How turbulence enhances coalescence of settling particles with applications to rain in clouds, Proc. R. Soc. A **461**, 3059 (2005).
[5] O. Ayala, B. Rosa, L.-P. Wang, and W. Grabowski, Effects of turbulence on the geometric collision rate of sedimenting droplets. part 1. results from direct numerical simulation, New J. Phys. **10**, 075015 (2008).
[6] J. Davila and J. Hunt, Settling of small particles near vortices and in turbulence, J. Fluid Mech. **440**, 117 (2001).
[7] J. Bec, H. Homann, and S. S. Ray, Gravity-Driven Enhancement of Heavy Particle Clustering in Turbulent Flow, Phys. Rev. Lett. **112**, 184501 (2014).
[8] K. Gustavsson, J. Jucha, A. Naso, E. Lévêque, A. Pumir, and B. Mehlig, Statistical Model for the Orientation of Nonspherical Particles Settling in Turbulence, Phys. Rev. Lett. **119**, 254501 (2017).
[9] P. Anand, S. S. Ray, and G. Subramanian, Orientation Dynamics of Sedimenting Anisotropic Particles in Turbulence, Phys. Rev. Lett. **125**, 034501 (2020).
[10] P. A. Vaillancourt and M. K. Yau, Review of particle-turbulence interactions and consequences for cloud physics, Bull. Am. Meteorol. Soc. **81**, 285 (2000).
[11] G. Falkovich, A. Fouxon, and M. G. Stepanov, Acceleration of rain initiation by cloud turbulence, Nature (London) **419**, 151 (2002).
[12] R. A. Shaw, Particle-turbulence interactions in atmospheric clouds, Annu. Rev. Fluid Mech. **35**, 183 (2003).
[13] E. Bodenschatz, S. P. Malinowski, R. A. Shaw, and F. Stratmann, Can we understand clouds without turbulence? Science **327**, 970 (2010).
[14] R. Monchaux, M. Bourgoin, and A. Cartellier, Analyzing preferential concentration and clustering of inertial particles in turbulence, Int. J. Multiph. Flow **40**, 1 (2012).
[15] A. J. Baran and P. N. Francis, On the radiative properties of cirrus cloud at solar and thermal wavelengths: A test of model consistency using high-resolution airborne radiance measurements, Q. J. R. Meteorol. Soc. **130**, 763 (2004).
[16] M. W. Gallagher, P. J. Connolly, J. Whiteway, D. Figueras-Nieto, M. Flynn, T. W. Choularton, K. N. Bower, C. Cook, R. Busen, and J. Hacker, An overview of the microphysical structure of cirrus clouds observed during EMERALD-1, Q. J. R. Meteorol. Soc. **131**, 1143 (2005).
[17] A. K. Pandit, H. S. Gadhavi, M. Venkat Ratnam, K. Raghunath, S. V. B. Rao, and A. Jayaraman, Long-term trend analysis and climatology of tropical cirrus clouds using 16 years of lidar data set over Southern India, Atmos. Chem. Phys. **15**, 13833 (2015).
[18] G. A. Voth and A. Soldati, Anisotropic particles in turbulence, Annu. Rev. Fluid Mech. **49**, 249 (2017).
[19] S. Alben, M. Shelley, and J. Zhang, Drag reduction through self-similar bending of a flexible body, Nature (London) **420**, 479 (2002).
[20] B. Marchetti, V. Raspa, A. Lindner, O. du Roure, L. Bergougnoux, E. Guazzelli, and C. Duprat, Deformation of a flexible fiber settling in a quiescent viscous fluid, Phys. Rev. Fluids **3**, 104102 (2018).
[21] A. A. Banaei, M. Rahmani, D. M. Martinez, and L. Brandt, Inertial settling of flexible fiber suspensions, Phys. Rev. Fluids **5**, 024301 (2020).
[22] F. Lundell, L. D. Soderberg, and P. H. Alfredsson, Fluid mechanics of papermaking, Annu. Rev. Fluid Mech. **43**, 195 (2011).
[23] D. K. A. Barnes, F. Galgani, R. C. Thompson, and M. Barlaz, Accumulation and fragmentation of plastic debris in global environments, Philos. Trans. R. Soc. B **364**, 1985 (2009).
[24] M. Stelfox, J. Hudgins, and M. Sweet, A review of ghost gear entanglement amongst marine mammals, reptiles and elasmobranchs, Mar. Pollut. Bull. **111**, 6 (2016).
[25] L. Lebreton, B. Slat, F. Ferrari, B. Sainte-Rose, J. Aitken, R. Marthouse, S. Hajbane, S. Cunsolo, A. Schwarz, A. Levivier, K. Noble, P. Debeljak, H. Maral, R. Schoeneich-Argent, R. Brambini, and J. Reisser, Evidence that the great pacific garbage patch is rapidly accumulating plastic, Sci. Rep. **8**, 4666 (2018).
[26] R. H. Luchsinger, B. Bergersen, and J. G. Mitchell, Bacterial swimming strategies and turbulence, Biophys. J. **77**, 2377 (1999).
[27] R. Stocker, Reverse and flick: Hybrid locomotion in bacteria, Proc. Natl. Acad. Sci. USA **108**, 2635 (2011).

[28] J. Jimenez, Oceanic turbulence at millimeter scales, Sci. Mar. **61**, 47 (1997).
[29] R. B. Bird, C. F. Curtiss, R. C. Armstrong, and O. Hassager, *Dynamics of Polymeric Liquids* (John Wiley and Sons, New York, 1977).
[30] C. Brouzet, G. Verhille, and P. Le Gal, Flexible Fiber in a Turbulent Flow: A Macroscopic Polymer, Phys. Rev. Lett. **112**, 074501 (2014).
[31] G. Verhille and A. Bartoli, 3D conformation of a flexible fiber in a turbulent flow, Exp. Fluids **57**, 117 (2016).
[32] J. R. Picardo, D. Vincenzi, N. Pal, and S. S. Ray, Preferential Sampling of Elastic Chains in Turbulent Flows, Phys. Rev. Lett. **121**, 244501 (2018).
[33] R. Singh, M. Gupta, J. R. Picardo, D. Vincenzi, and S. S. Ray, Elastoinertial chains in a two-dimensional turbulent flow, Phys. Rev. E **101**, 053105 (2020).
[34] J. R. Picardo, R. Singh, S. S. Ray, and D. Vincenzi, Dynamics of a long chain in turbulent flows: impact of vortices, Philos. Trans. R. Soc. A **378**, 20190405 (2020).
[35] M. E. Rosti, A. A. Banaei, L. Brandt, and A. Mazzino, Flexible Fiber Reveals the Two-Point Statistical Properties of Turbulence, Phys. Rev. Lett. **121**, 044501 (2018).
[36] S. Allende, C. Henry, and J. Bec, Stretching and Buckling of Small Elastic Fibers in Turbulence, Phys. Rev. Lett. **121**, 154501 (2018).
[37] T. B. Oehmke, A. D. Bordoloi, E. Variano, and G. Verhille, Spinning and tumbling of long fibers in isotropic turbulence, Phys. Rev. Fluids **6**, 044610 (2021).
[38] S. Jin and L. R. Collins, Dynamics of dissolved polymer chains in isotropic turbulence, New J. Phys. **9**, 360 (2007).
[39] R. M. Jendrejack, J. J. de Pablo, and M. D. Graham, Stochastic simulations of dna in flow: Dynamics and the effects of hydrodynamic interactions, J. Chem. Phys. **116**, 7752 (2002).
[40] C. M. Schroeder, E. S. G. Shaqfeh, and S. Chu, Effect of hydrodynamic interactions on DNA dynamics in extensional flow: Simulation and single molecule experiment, Macromolecules **37**, 9242 (2004).
[41] M. Cosentino Lagomarsino, I. Pagonabarraga, and C. P. Lowe, Hydrodynamic Induced Deformation and Orientation of a Microscopic Elastic Filament, Phys. Rev. Lett. **94**, 148104 (2005).
[42] X. Schlagberger and R. R. Netz, Orientation of elastic rods in homogeneous stokes flow, Europhys. Lett. **70**, 129 (2005).
[43] I. Llopis, I. Pagonabarraga, M. Cosentino Lagomarsino, and C. P. Lowe, Sedimentation of pairs of hydrodynamically interacting semiflexible filaments, Phys. Rev. E **76**, 061901 (2007).
[44] B. Delmotte, E. Climent, and F. Plouraboué, A general formulation of bead models applied to flexible fibers and active filaments at low Reynolds number, J. Comput. Phys. **286**, 14 (2015).
[45] R. G. Cox, The motion of long slender bodies in a viscous fluid Part 1. General theory, J. Fluid Mech. **44**, 791 (1970).
[46] X. Xu and A. Nadim, Deformation and orientation of an elastic slender body sedimenting in a viscous liquid, Phys. Fluids **6**, 2889 (1994).
[47] Y. Dubief and F. Delcayre, On coherent-vortex identification in turbulence, J. Turbul. **1**, N11 (2000).
[48] M. James and S. S. Ray, Enhanced droplet collision rates and impact velocities in turbulent flows: The effect of poly-dispersity and transient phases, Sci. Rep. **7**, 12231 (2017).
[49] H. C. Öttinger, *Stochastic Processes in Polymeric Fluids* (Springer, Berlin, 1996).
[50] F. Bagheri, D. Mitra, P. Perlekar, and L. Brandt, Statistics of polymer extensions in turbulent channel flow, Phys. Rev. E **86**, 056314 (2012).
[51] T. Berk and F. Coletti, Dynamics of small heavy particles in homogeneous turbulence: A Lagrangian experimental study, J. Fluid Mech. **917**, A47 (2021).
[52] S. Gerashchenko and V. Steinberg, Statistics of Tumbling of a Single Polymer Molecule in Shear Flow, Phys. Rev. Lett. **96**, 038304 (2006).
[53] A. Celani, A. Puliafito, and K. Turitsyn, Polymers in linear shear flow: A numerical study, Europhys. Lett. **70**, 464 (2005).
[54] S. N. Majumdar, C. Sire, A. J. Bray, and S. J. Cornell, Nontrivial Exponent for Simple Diffusion, Phys. Rev. Lett. **77**, 2867 (1996).

[55] B. Derrida, V. Hakim, and R. Zeitak, Persistent Spins in the Linear Diffusion Approximation of Phase Ordering and Zeros of Stationary Gaussian Processes, Phys. Rev. Lett. **77**, 2871 (1996).
[56] S. N. Majumdar, Persistence in nonequilibrium systems, Curr. Sci. **77**, 370 (1999).
[57] A. J. Bray, S. N. Majumdar, and G. Schehr, Persistence and first-passage properties in nonequilibrium systems, Adv. Phys. **62**, 225 (2013).
[58] P. Perlekar, S. S. Ray, D. Mitra, and R. Pandit, Persistence Problem in Two-Dimensional Fluid Turbulence, Phys. Rev. Lett. **106**, 054501 (2011).
[59] B. Kadoch, D. del-Castillo-Negrete, W. J. T. Bos, and K. Schneider, Lagrangian statistics and flow topology in forced two-dimensional turbulence, Phys. Rev. E **83**, 036314 (2011).
[60] A. Bhatnagar, A. Gupta, D. Mitra, R. Pandit, and P. Perlekar, How long do particles spend in vortical regions in turbulent flows? Phys. Rev. E **94**, 053119 (2016).
[61] M. Valyrakis, P. Diplas, and C. L. Dancey, Entrainment of coarse grains in turbulent flows: An extreme value theory approach, Water Resour. Res. **47**, W09512 (2011).
[62] E. Gauger and H. Stark, Numerical study of a microscopic artificial swimmer, Phys. Rev. E **74**, 021907 (2006).